Mechanistic study of hydrazine decomposition on Ir(111)

Mechanistic study of hydrazine decomposition on Ir(111)

Xiuyuan Lu[a], Samantha Francis[a], Davide Motta[a], Nikolaos Dimitratos[b]*, Alberto Roldan[a]*

[a] Cardiff Catalysis Institute, School of Chemistry, Cardiff University, Main Building, Park Place, Cardiff, CF10 3AT, UK

[b] Department of Industrial Chemistry "Toso Montanari"; Alma Mater Studiorum-University of Bologna; Viale Risorgimento, Bologna, Italy

Abstract:

Hydrogen transport and storage technology remain one of the critical challenges of the hydrogen economy. Hydrazine (N_2H_4) is a carbon-free hydrogen carrier which has been widely used as fuel in the field of space exploration. We have combined experiments and computer simulations in order to gain a better understanding of the N_2H_4 decomposition on Ir catalyst, the most efficient catalyst for hydrazine decomposition up to date. We have identified metallic Ir rather than IrO_2 as the active phase for hydrazine decomposition and carried out density functional theory (DFT) calculations to systematically investigate the changes in the electronic structure along with the catalytic decomposition mechanisms. Three catalytic mechanisms to hydrazine decomposition over Ir(111) have been found: (i) intramolecular reaction between hydrazine molecules, (ii) intramolecular reaction between co-adsorbed amino groups, and (iii) hydrazine dehydrogenation assisted by co-adsorbed amino groups. These mechanisms follow five different pathways for which transition states and intermediates have been identified. The results show that hydrazine decomposition on Ir(111) starts preferentially with an initial N-N bond scission followed by hydrazine dehydrogenation assisted by the amino produced, eventually leading to ammonia and nitrogen production. The preference for N-N scission mechanisms was rationalized by analyzing the electronic structure. This analysis showed that upon hydrazine adsorption, the π bond between nitrogen atoms becomes weaker.

Keywords: heterogeneous catalysis, hydrazine, ammonia, hydrogen, decomposition mechanism, density functional theory

1. Introduction

In recent years, air pollution, global warming and new legislation are increasing the demand for low-carbon energy. Hydrogen has been recognized as a clean fuel with high power density, which, in combination with efficient fuel cells, could supply enough power to minimize the current environmental pressure.[1] However, hydrogen transport and storage technology remain one of the critical challenges of the hydrogen economy. At present, it is very difficult to find novel materials with a high hydrogen storage capacity, and attention is being paid to molecular storage systems such as alcohols, formic acid, ammonia and hydrazine.

Hydrazine (N_2H_4) is a carbon-free hydrogen carrier with 12.5 wt% hydrogen content, it remains liquid between 2 and 114 °C and is stable in aqueous solutions. As early as 1970, Raschig developed the first commercial process to produce hydrazine, and now, there are many mature processes to produce it, e.g. from urea, Bayer Ketazine and peroxide processes.[2,3] Especially, recent research has demonstrated the promise of producing hydrazine via microbial conversion of biomass.[4] N_2H_4 is widely used in the manufacturing of agrochemicals, rubber production and space exploration related industries. In the latest case, N_2H_4 is used as a propellant fuel for space vehicles and satellites due to the highly exothermic decomposition reactions (***Path*** 1 and ***Path*** 2) generating gaseous products, i.e. N_2, H_2 and NH_3.[5]

$$N_2H_4 \rightarrow N_2 + 2H_2 \qquad \Delta G(273K) = -1.46\ eV \qquad \text{Path 1}$$

$$N_2H_4 \rightarrow 4/3NH_3 + 1/3N_2 \qquad \Delta G(273K) = -1.72\ eV \qquad \text{Path 2}$$

The decomposition process does not strictly follow stoichiometric paths as it is affected by many factors including the nature of the catalyst and the reaction temperature.[6] Since the catalyst strongly determines the activity and selectivity of the process, there have been several studies to develop efficient catalysts for hydrazine decomposition. The earliest commercialized catalyst for hydrazine dissociation consisted of supported Ir particles on γ-alumina (Ir/γ-Al_2O_3). This catalyst was used in spacecraft control thrusters for spontaneous ignition and stability.[7] Cho *et al*. prepared high loading Ir/γ-Al_2O_3 catalysts with multiple impregnation methods and investigated the decomposition of hydrous hydrazine. They found that the catalysts were able to show high hydrogen selectivity only under reaction temperatures above 200 °C.[8] Aika *et al*. investigated the decomposition mechanism on Ir by a micro-catalytic gas chromatographic technique at ~150 °C and showed that the products were only NH_3 and N_2.[5] With the aims to make the catalyst more affordable and widening its applications, Xu *et al*. synthesized a series of mono- and bimetallic nanoparticles (Rh, Co, Ru, Ir, Fe, Cu, Ni, Pt, Pd) and tested their catalytic activity for hydrazine decomposition.[9–11] The synergistic effect and electron transfer between metals in the alloys improved the H_2 selectivity and activity of the decomposition reaction. Manukyan *et al*. prepared Cu nanoparticles covered by a FeNi alloy, for which hydrogen selectivity reached 100% at 70 °C.[12] Maurel *et al.* studied ^{15}N-labeled hydrazine decomposition on transition metals and found that N_2 is always formed from a single hydrazine molecule without any N-N bond breakage or N scrambling under the range of temperature 60 – 300 °C.[13] Although these precedent works bring insights to the possible reaction pathway, a complete understanding of the catalytic process is still ambiguous and controversial. Computational simulations can provide an atomistic approach to identify the role of the metal

active sites along the reaction pathways.

Computational studies have described the full network of reaction pathways in the N_2H_4 decomposition process on metal catalysts. Electronic structure calculations showed that the N_2H_4 dehydrogenation process on terraced and stepped Cu(111) surface and on Rh(111) takes place between co-adsorbed NH_2 resulting from N–N scissions and adsorbed N_2H_x (x = 1-4) dehydrogenation.[14,15]

Thus far, the Ir-based catalysts remain as the standard for the decomposition of hydrazine although systematic mechanistic information on the decomposition mechanism over Ir is scarce.[16] For this reason, we have performed accurate simulations including dispersion corrections following three different catalytic mechanisms: (i) intramolecular reaction between hydrazine, (ii) intramolecular reaction between co-adsorbed NH_2, and (iii) hydrazine dehydrogenation assisted by co-adsorbed NH_2 groups.[17] We also provide a comprehensive rationalization of the decomposition process on Ir(111) on its electronic structure, which agrees with our experiment results.

2. Computational methods

All calculations have been carried out by the Vienna Ab-initio Simulation Package (VASP) utilizing spin-polarized density functional theory (DFT).[18,19] The exchange-correlation energy was calculated using the Perdew-Burke-Ernzerhof (PBE)[20] form of the generalized gradient approximation (GGA),[21] and the effect of inner cores, including non-spherical contributions to the gradient corrections, were represented by the projector augmented wave (PAW).[21,22] To improve the description of the long-range interaction, we employed the zero damping DFT-D3 method of Grimme,[23] which has been proven to be an upgrade on several systems.[24–26] We used plane-wave basis sets with a kinetic energy cutoff of 500 eV. Optimized structures were converged within a threshold of internal forces smaller than 0.02 eV/Å with the conjugate gradient algorithm and an electronic relaxation threshold of 10^{-5} eV.

The calculated lattice parameter for iridium is 3.843 Å, which is in good agreement with the experimental value of 3.839 Å.[27] The surface was represented by a p(4x4) supercell slab model with 5 atomic layers, where the top three were fully relaxed and the bottom fixed at the bulk lattice. Different slab thicknesses for Ir and IrO_2 were tested until convergence was achieved within 1 meV per atom. The Brillouin zone was sampled by a Γ-centered $3\times3\times1$ Monkhorst-Pack grid with Methfessel-Paxton smearing broadening of σ = 0.2 eV to acquire an accurate description of the total energy. A vacuum of 15 Å was added perpendicular to the surface to avoid spurious interaction with periodic images. Upon molecular interaction, dipole correction along the z-direction was applied to enhance the energy convergence.

There are three main conformations of hydrazine in the gas phase, i.e. gauche, trans and eclipsed. The energy of trans and eclipsed conformations are 0.13 and 0.36 eV higher than the gauche conformation, respectively.[14] Hence, we used the energy of the gauche conformation as the gas-phase N_2H_4 energy to calculate its adsorption energy and the relative values of intermediates along with the energy profiles according to ***Eq 1***.

$$E^{ads}_{N_yH_x} = \left(E^{surf}_{N_yH_x} + (4-x)E^{surf}_{H} + (2-y)E^{surf}_{N}\right) - \left(((4-x)+(2-y)+1)E^{surf} + E^{gas}_{N_2H_4}\right) \qquad \text{Eq 1}$$

Where E^{surf}_{NyHx} denotes the total energy of the adsorbed N_yH_x on a surface, E^{surf}_{H} and E^{surf}_{N}

are, respectively, the energies of an adsorbed atom of hydrogen and nitrogen on the surface. Additionally, E^{surf} and E_{N2H4}^{gas} represent the energy of the naked surface and an isolated hydrazine molecule in the gas phase.

We combined the climb-image nudged elastic band (ci-NEB)[28,29] and the improved dimer method (IDM)[30] to find the saddle point of the transition states (TS), making sure that there is a unique imaginary frequency along with the reaction coordinate. The reaction energy (E_r) is given by the difference between the final state (FS) energy and the initial state (IS) energy (***Eq 2***). Thus, a negative value means an exothermic step. We defined the forward and reverse activation barriers (E_a) as the energy difference represented by ***Eq 3*** and ***Eq 4***.

$$E_r = E_{FS} - E_{IS} \quad \text{Eq 2}$$

$$E_a(\text{forward}) = E_{TS} - E_{IS} \quad \text{Eq 3}$$

$$E_a(\text{reverse}) = E_{TS} - E_{FS} \quad \text{Eq 4}$$

3. Experimental methods

3.1 Materials

There are six primary reagents used in the experiment. Hydrazine monohydrate (reagent grade, 98%, cat. 207942) is obtained from Sigma-Aldrich, sodium hydroxide (pellets, cat. 30620-1KG) from Fluka, hydrochloric acid (conc. 37%, cat. 258148) from Sigma-Aldrich, iridium chloride (99.95%, cat. 12184.06) from Alfa aesar, cerium oxide nano-powder (particles size <25nm, cat. 544841) from Sigma-Aldrich and urea (powder, Bioreagent, cat. U5378).

3.2 Catalyst preparation

The deposition precipitation method has been employed to prepare the monometallic Ir catalyst. The metal precursor $IrCl_4 \cdot H_2O$ was dissolved to 400 mL solution to ensure 10 mg of iridium on the final catalyst. Then, 10.06 g urea was added in solution to keep a pH of 4.10, and 0.990 g of CeO_2 were dispersed in the solution as support. This solution was warm up to 80°C and left till the pH remained constant at around 7 for 4 hours. The synthesized catalyst was filtrated and dried in an oven at 110°C; part of the catalyst was then kept for catalytic studies. Afterwards, the remaining catalysts were heat-treated in air at 400°C for 3 hours and later treated in 10% H_2/Ar mixture at 600°C for 6 hours.

3.3 Catalytic tests

The performances of the catalytic materials were studied using a volumetric gas displacement system, which consisted of a tightly sealed round bottom flask connected to an acid trap and a gas burette to measure the volume of produced gas. 8 mL of 0.5M NaOH solution was brought at 50°C with 76.2 mg of 1 wt.% Ir/CeO_2 under stirring. After that, 0.3 mL of 3.3M hydrazine solution was added, and the system was purged with N_2 without stirring. Finally, stirring was started to prompt the reaction.

The gases produced by the reaction passed through a solution of HCl to trap any gaseous ammonia present in the stream. The moles of gas produced were then calculated and used to quantify the final yield of H_2 production reaction, ***Eq 5***. Blank comparisons were performed to

prove the stability of the hydrazine solution in absence of catalysts and quantify the gases produced by the mixed reactants.

$$\text{H Yield} = \frac{3 * \frac{nH_2 + nN_2}{nN_2H_4\ \text{initial}} - 1}{8} * 100 \qquad \text{Eq 5}$$

Where H yield is in percentage, $nH_2 + nN_2$ are total moles of gas produced, nN_2H_4 initial are the moles of hydrazine at the beginning of the reaction.

The experimental tests were performed at least three times in the same conditions in order to validate the data obtained.

3.4 Characterization

Scanning electron microscope (SEM) was performed to study the morphology and content of iridium on the sample. The images were taken on Hitachi TM3030PLUS (Tokyo, Japan) equipped with Quantax70 Energy-Dispersive X-ray spectroscopy (EDX).

SEM-EDX allowed the quantification of the Ir element on the samples (0.98 ± 0.05 wt.%), which is close to the theoretical loading value of 1 wt.%. ***Figure 1*** displays the distribution of the active metal on the support that appears to be homogeneous among the surface.

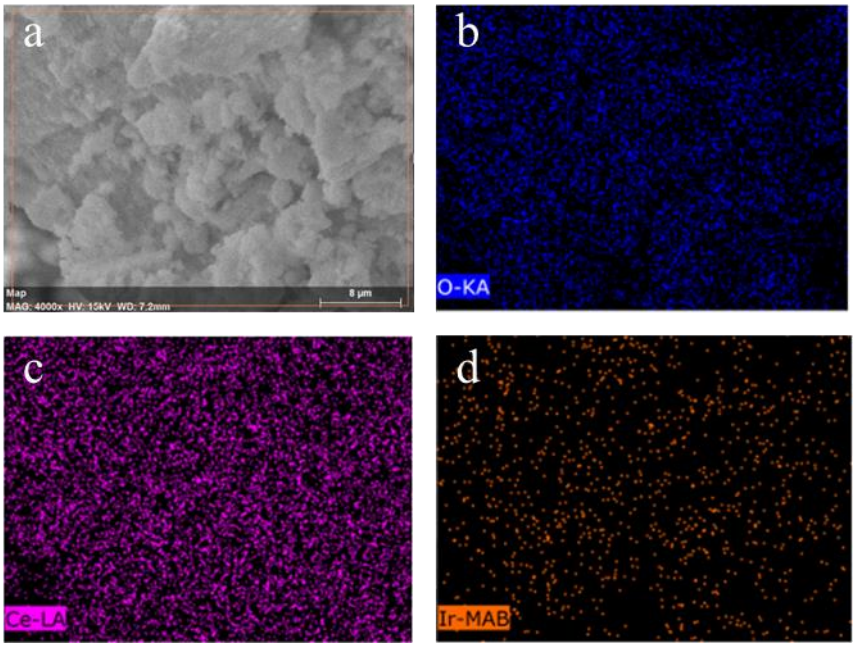

Figure 1. a) SEM image of Ir/CeO_2, b-d) the EDS mapping of its surface for the main element present in the catalyst.

X-Ray diffraction (XRD) analyses were performed with PANanalytical X'PertPRO X-ray diffractometer (Almelo, The Netherlands) using Cu K radiation and worked at 40 kV and 30 mA. The diffraction patterns were recorded between 10 °– 80 ° 2θ at a step size of 0.017 °.

For metallic iridium, the diffraction peaks at 2θ of 40.8 °, 47.2 °, 69.1 ° and 83.6 ° correspond to the (111), (200), (220) and (311) planes respectively, which are the most stable forms for Ir. While the X-ray diffract at 2θ of 28.1 °, 35.0 °, 39.8 ° and 55.3 ° correspond to IrO_2 surface of

(110), (101), (200) and (211) respectively. ***Figure 2*** does not exhibit any these peaks but only the CeO_2 pattern, 2θ = 29.3 °, 33.1 °, 47.5 ° and 57.6 ° for (111), (200), (220) and (311) planes respectively.

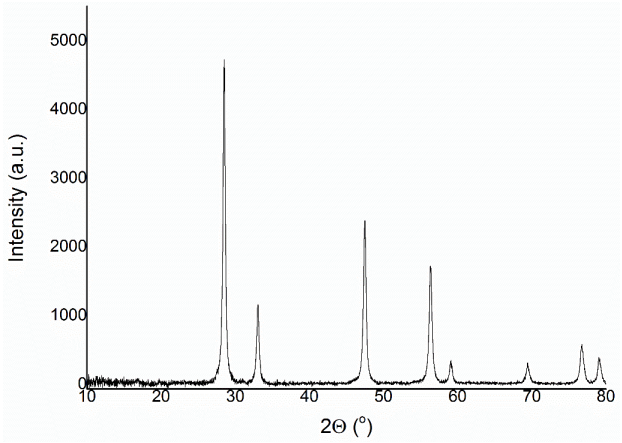

Figure 2. X-Ray diffraction pattern for Ir/CeO_2

X-ray photoelectron spectroscopy (XPS) was performed on a Kratos axis ultra-equipped with a delay line detector photoelectron spectrometer using monochromatic AlKα radiation (12 mA, 12 kV). The signal was averaged from a surface area of approximately 700×300 μm. Compensation of the charges on the insulated samples was achieved using the Kratos immersion lens and then setting the C 1s peak at 284.8 eV. The analysis of the data was done by CasaXPS (v2.3.17, Teignmouth, UK).

XPS (***Figure 3***) was performed to analyze the dried Ir/CeO_2 and reduced Ir/CeO_2 samples followed by H_2/Ar flow at 600°C allowing us to confirm the oxidation state of the active metal on the surface. The 4f region in ***Figure 3*** shows that two patterns are convoluted in two pair of peaks. One pattern is for the metallic iridium, $4f_{7/2}$ BE of 61.0 eV, while the other stands for Ir^{4+} and $4f_{7/2}$ BE of 62.0 eV, in agreement with previous reports.[31] The deconvolution of the spectrum reveals that the metallic iridium constitutes 70.6% of all superficial iridium in the reduced catalyst, whereas it constitutes only 8.6% of the total iridium on the surface without the reduction heat treatment.

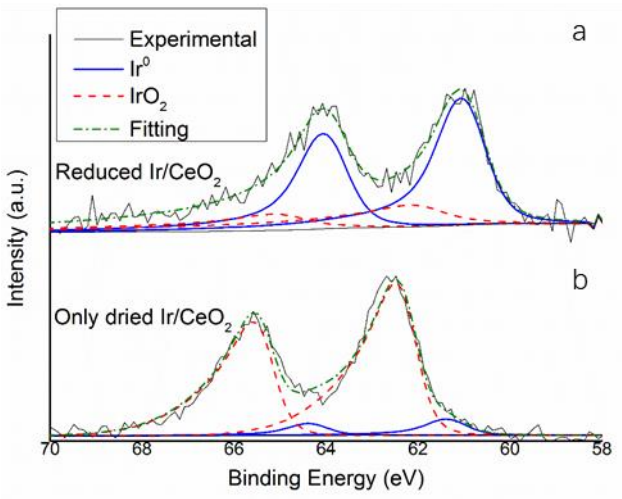

Figure 3. XPS spectrum of Ir 4f region for Ir/CeO_2 with deconvolution for metallic Ir and

iridium oxide, a) after and b) before the heat treatment.

4 Results and Discussion

Of the three major conformations of isolated hydrazine, gauche has presented as the most stable. Upon optimization, the molecule presented bond lengths of 1.450 Å for N–N and an average N–H bond of 1.020 Å. We studied its adsorption on IrO_2 surfaces and Ir(111) owing to the possible presence of an IrO_2 surface under typical reaction conditions.

4.1 Adsorption on the IrO_2 surface

We optimized the IrO_2 low Miller index surfaces (001), (100), (110) (101) and (111) and calculated their surface energies using the equation (***Eq 6***).

$$\gamma_{hkl} = \frac{E_{slab,hkl}^{relaxed} - E_{bulk}}{A_{hkl}} - \frac{E_{slab,hkl}^{unrelaxed} - E_{bulk}}{2A_{hkl}} \qquad \text{Eq 6}$$

Where γ_{hkl} is the surface energy of the slab, E_{bulk} is the total energy of the bulk, N is the number of bulk units in the slab, and finally, A_{hkl} is the (hkl) surface area. It was determined that the stability of IrO_2 surfaces follows the order (101) > (110) > (100) > (001) > (111), which is in agreement with previous studies, [32] see ***Table S1***. Once the most stable (101, 110 and 100) slabs were optimized, we adsorbed the molecules of N_2H_4, NH_3 and the atoms N and H on non-equivalent sites. The most stable geometries are represented in ***Figure S3***. Adsorption energies are calculated using ***Eq 7*** and are shown in ***Table 1***.

$$E_{ads} = E_{mol+surf} - (E_{surf} + E_{mol}) \qquad \text{Eq 7}$$

Where E_{ads} is the energy of adsorption, $E_{mol+surf}$ is the energy of the molecule/atom adsorbed on the surface, E_{surf} is the energy of the naked surface and E_{mol} is the energy of the molecule in the gas phase. The references for N and H adsorptions are half the total energies of gas phase nitrogen and hydrogen molecule respectively.

Table 1: The calculated adsorption energies of N_2H_4, NH_3, N and H on the most stable sites of IrO_2((101), (110) and (100)).

Adsorbate	E_{ads} (eV)		
	(101)	(110)	(100)
N	-3.16	-3.65	-3.92
H	-3.13	-3.57	-3.46
NH_3	-2.02	-2.46	-2.69
N_2H_4	-2.35	-3.24	-2.81

The adsorption energies in ***Table 1*** indicate that any of the three surfaces considered will adsorb N_2H_4 very strongly. The relative adsorption energies between N_2H_4 and atomic N and H shows that on the (101) surface, and in lower extent on the (110), hydrazine decomposition into

N and H is thermodynamically favorable. Nevertheless, the strong adsorption of these species will irreversibly occupy the adsorption site. To verify the IrO_2 caused deactivation, a decomposition test of hydrazine over the Ir/CeO_2 sample was performed. The reaction was followed at 50°C by the volume of the gas collected in a gas burette. The yield was calculated from the produced gaseous species according to ***Eq 5*** and was represented in ***Figure 4***. The catalyst without reduction heat treatment (mainly IrO_2) exhibit negligible catalytic activity to the hydrazine decomposition. These results are also in line with previous experimental results, the efficacy of an Ir catalyst toward hydrazine decomposition diminished upon its oxidation.[33] This result validates our DFT calculations made for the IrO_2 surface, which means only metallic iridium play a role in the hydrazine decomposition over Ir catalyst.

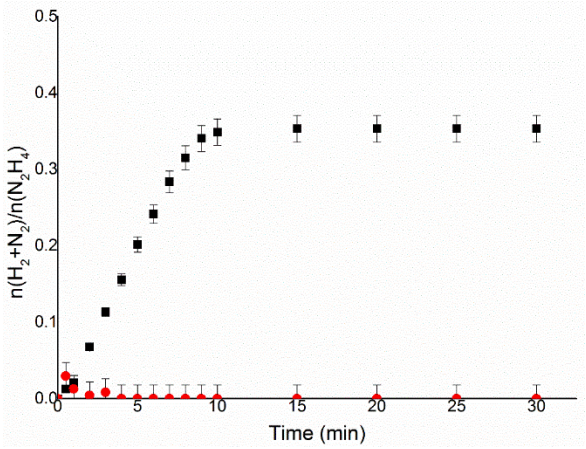

Figure 4. $n(H_2+N_2)/n(N_2H_2)$ versus time for hydrous hydrazine decomposition over Ir/CeO_2 using 0.3mL of 3.3M hydrazine monohydrate in 8mL 0.5M of NaOH solution, at 50°C and 76.2 mg of catalyst, for a substrate/metal ratio of 250, with a stirring rate of 1050 rpm. Black squared measurements correspond to reduced samples, while red circles indicate the non-reduced sample.

Figure 4 also includes information regarding stoichiometry at the equilibrium reaction. For the hydrazine decomposition over Ir/CeO_2, the $n(H_2+N_2)/n(N_2H_4)$ increased to about 1/3 after equilibrium and only a small fraction of hydrogen been obtained in the reaction product. This result shows that the hydrazine decomposition on Ir follows ***Path*** 2 under our experimental conditions. Based on these results, we analyzed the structures and energies of all the species on the Ir(111) to elaborate on the different reaction pathway.

4.2 Species on Ir(111) surface

The most stable *fcc* Ir surface is the close-packed (111) in which atoms are arranged in a hexagonal lattice with a separation of 2.692 Å. We investigated several adsorption geometries on the surface for the different species along with the three reaction mechanisms and described the most stable below.

N_2H_4. We approached the hydrazine gauche conformation to four non-equivalent sites, i.e. top, bridge, and fcc and hcp hollow, with parallel and perpendicular orientations on the clean Ir(111) surface in order to identify the most stable adsorption geometry, see ***Figure 5a***. The molecule binds through both nitrogen atoms almost parallel to the flat surface in a bridge site with an Ir-N average distance of 2.137 Å. Exothermic adsorption of 2.70 eV (shown in ***Table 2***)

elongates the N–N bond to 1.472 Å from 1.450 Å in the gauche conformation, while the distance of N–H bonds shorten to 0.977 Å from the original 1.024 Å. Similar results were found by Agusta *et al*. investigated N_2H_4 adsorption on Ni(111) and suggested the anti-conformation as the most stable configuration during the hydrazine adsorption but the cis-conformation as a transition state for the decomposition reaction.[34]

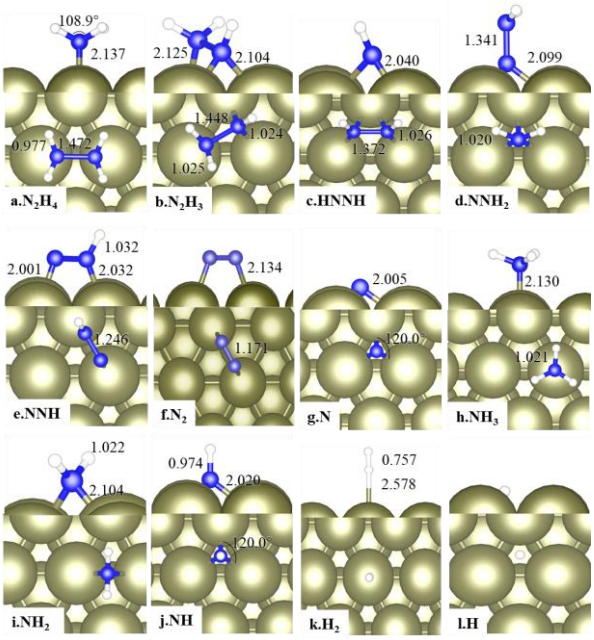

Figure 5. Side and Top view of adsorbed N_2H_x (x = 0-4), NH_x (x = 0-3) and H species on the Ir(111) surface (side view and top view). All distances inset are in Å. Blue spheres represent N atoms, white is hydrogen, and Ir is the large green sphere.

Table 2. Adsorption energies (E_{ads}) and average bond lengths (d), including coordination (η), of the adsorbed species on the Ir(111). We added the isolated hydrazine molecule in the gas phase for comparison.

Adsorbate	**E_{ads} (eV)**	**d(Ir–N^1) (Å)**	**d(Ir–N^2) (Å)**	**d(N^1–N^2) (Å)**	**d(N^1–H) (Å)**	**d(N^2–H) (Å)**
N_2H_4 gas	--	--	--	1.450	η (2); 1.020	η (2); 1.020
N_2H_4	-2.70	2.137	2.137	1.472	η (2); 0.977	η (2); 0.977
N_2H_3	-2.97	2.125	η (2); 2.104	1.448	η (2); 1.025	1.024
HNNH	-2.47	η (2); 2.040	η (2); 2.040	1.372	1.026	1.026
NNH_2	-2.79	η (3); 2.099	-	1.341	-	η (2); 1.020
NNH	-3.06	2.032	2.011	1.246	1.032	-
NH_3	-1.95	2.130	-	-	η (3); 1.021	-
NH_2	-3.72	2.104	-	-	η (2); 1.022	-
NH	-4.31	η (3); 2.020	-	-	0.974	-
N_2	-1.14	2.134	2.134	1.171	-	-
H_2	-0.53	-	-	-	-	-
N	-0.56	η (3); 2.005				
H	-0.86	-	-	-	-	-

We have carried out an analysis of the electron density arrangement to characterize the

bonding between the hydrazine and the Ir(111) surface. ***Figure 6*** shows the charge density flux calculated as the difference between the charge density of the total adsorbate system and the sum of the charge densities of the molecule and the clean surface in the same geometry (***Eq 8***). Upon N_2H_4 adsorption, the charge density accumulates between N–Ir bonds leading to sp^3 hybridisation of the N orbitals and the weakening of the N–N bond, which is in line with its elongation from the gas phase geometry. This electronic rearrangement breaks the planarity of the molecule, as noticed in ***Figure 5a.***

$$\rho_{transfer} = \rho_{surf+molecule} - (\rho_{surf} + \rho_{molecule}) \qquad \text{Eq 8}$$

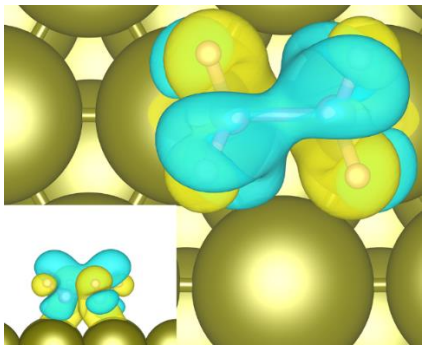

Figure 6. Top and side view (inset) of the partial charge density flow upon N_2H_4 adsorption. Yellow and blue iso-surfaces (0.01 e/Å^3) denote gain and depletion of electron density, respectively. Blue spheres represent N atoms, white is hydrogen, and Ir is the large green sphere.

We also employed the density of states (DOS) and the Bader charge analysis to characterize the N–Ir interaction. Their analysis showed that one N_2H_4 molecule donates 0.6 e^- to the Ir(111) surface during the adsorption process, see ***Table S2*** for atomic charges. Moreover, the DOS shows how the electronic structure is affected by the interactions between the surface and adsorbate. ***Figure 7*** helps to compare the DOS of the naked surface and isolated molecule with the adsorbed system. It shows a clear shift to lower energies of the N_2H_4 orbitals. In particular, the antibonding orbital (π^*) moves below the Fermi energy, which decreases the N–N bond order agreeing with the bond elongation previously observed. Initially, one may think that it contradicts the charge transfer, i.e. from the molecule to the surface, even though, this is a common case where the electron rearrangement leads to back-donation into the antibonding orbital.[35]

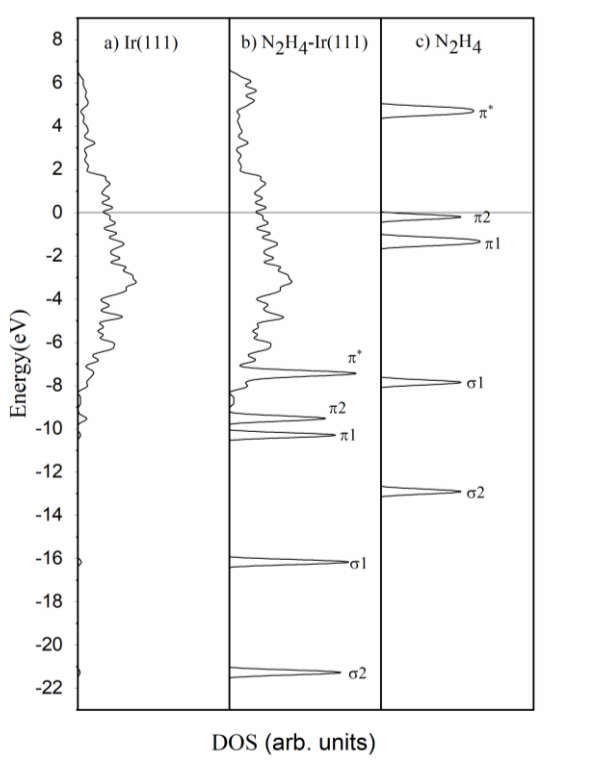

Figure 7. The total density of states of a) bare Ir(111), b)N_2H_4/Ir(111) and c) isolated gauche N_2H_4. The horizontal line across diagrams represents the common Fermi energy.

Once N_2H_4 is adsorbed, we explored the adsorption sites and geometry of the different intermediates, included in **Figure 5** and **Table 2**. Independently of the adsorbed species, the distances between surface atoms remains practically unchanged. We further developed the discussion and comparison with previous reports in the Supplementary Information. In brief, these intermediate species increase their coordination with the surface as the dehydrogenation proceeds and, in general, the adsorption becomes less favourable and the N-N bond stronger and shorter, in agreement with the vibrational shift (see below).

4.3 N_2H_4 decomposition pathways on Ir(111)

In the following section, we have discussed the elementary reaction steps for each mechanism of the catalytic decomposition of N_2H_4 on Ir(111). Forward and backward energy reactions and activation energies are summarized in ***Table 3***. We have listed the frequencies related to the reaction coordinate of all the reactions across the different mechanisms in ***Table S3***. Nearly all imaginary vibrations modes are stretching expect the dehydrogenation of NNH*, which is a N-H bending.

Dehydrogenation. Starting with N_2H_4, the process of breaking an N–H bond and placing H on the most stable surface site is endothermic (E_r= 0.18 eV) with an energy barrier (activation energy) of 1.08 eV. The process is schematically represented in ***Figure 8a***. This first step leads to N_2H_3 (see the energy profile ***Figure 13***), which following dehydrogenation derives into

symmetrically or asymmetrically species. The asymmetric path (***Figure 8b***) is endothermic by 0.57 eV with an activation energy of 1.02 eV, making it highly improbable. The symmetric step (***Figure 8c***) is also endothermic (0.54 eV) and leads to HNNH and an H ad-atom upon overtaking a significant barrier of 2.05 eV.

HNNH is the symmetric product of the N_2H_3 dehydrogenation, and the following dehydrogenation step leads to N_2H, which lies 0.19 eV below reactants after overtaking a barrier of 0.70 eV (***Figure 8e***). It is the most feasible intramolecular dehydrogenation reaction of any intermediate on the Ir(111) surface. The asymmetric intermediate (NNH_2) requires overtaking an energy barrier of 0.83 eV to produce N_2H, see ***Figure 8d***. The decomposition of N_2H_2 on Ir(111) is more favorable than on Cu(111),[14] which has higher barrier energies of 1.35 eV for NNH_2 and 1.68 eV for N_2H. Its subsequent dehydrogenation (***Figure 8f***) towards N_2 and H has a high energy barrier of 1.31 eV and the products lie only 0.02 eV below, making the process energetically unfavorable.

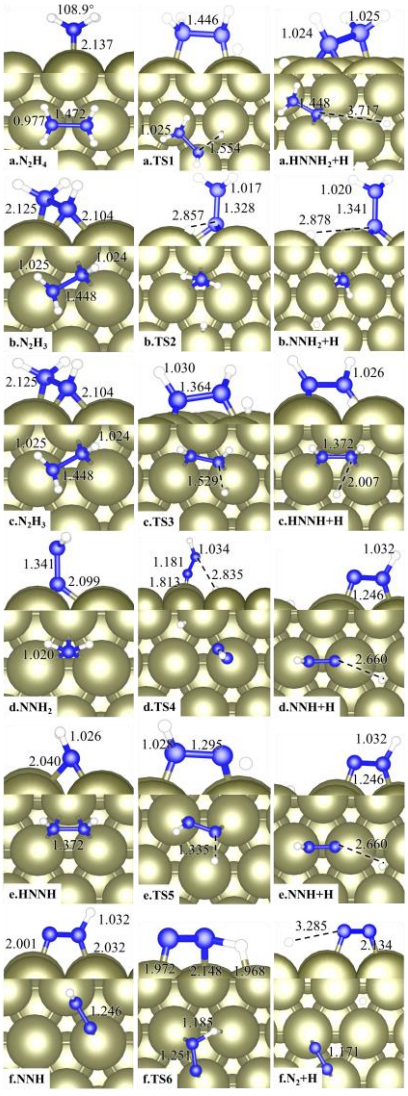

Figure 8. Top and side views of the initial, transition and final states for the dehydrogenation pathways: a) N_2H_4 dehydrogenation, b) N_2H_3 dehydrogenation to NNH_2, c) N_2H_3

dehydrogenation to HNNH, d) NNH_2 dehydrogenation, e) HNNH dehydrogenation, f) NNH dehydrogenation. All inset distances are in Å. Blue spheres represent N atoms, white is hydrogen, and Ir is the large green sphere.

N–N dissociation. The exothermic breaking of the hydrazine N–N bond (E_r= -0.52 eV) leads to the formation of amino species (NH_2) with an energy barrier of 0.71 eV, see ***Figure 9a***. In comparison with the dehydrogenation pathway, the dissociation is more energetically favorable in agreement with previous studies.[13] Nevertheless, the results are not as favorable as previously reported (E_a= 0.52 eV and E_r= -0.93 eV)[16] due to the dispersion corrections included. It has been largely proven that including dispersion corrections, even by semi-empirical methods, leads to more accurate description of molecular interactions since effects like dipoles, e.g. in absorbed hydrazine and NH_2, are not otherwise considered.

Resulting from an initial dehydrogenation, N_2H_3 breaks the N–N bond (***Figure 9b***) through an energy barrier of 0.78 eV leading to NH and NH_2 species on the surface. These species lie at 0.71 eV below the energy value of the initial state. Again, the N-dissociation path is energetically more favorable than the dehydrogenations steps. Similarly, the scission of N–N on the asymmetric N_2H_2 requires 0.73 eV to overtake the energy barrier leading to NH_2 species and N on the surface 0.53 eV below the initial state (***Figure 9c***). The N-dissociation of the symmetric N_2H_2 (***Figure 9d***) is thermodynamically more favorable than the asymmetric by 0.96 eV with the same E_a= 0.73 eV. The dissociation to N and NH intermediates from N_2H (***Figure 9e***) is driven by the formation of products (E_r= -1.21 eV) but prevented by a high energy barrier of 1.43 eV.

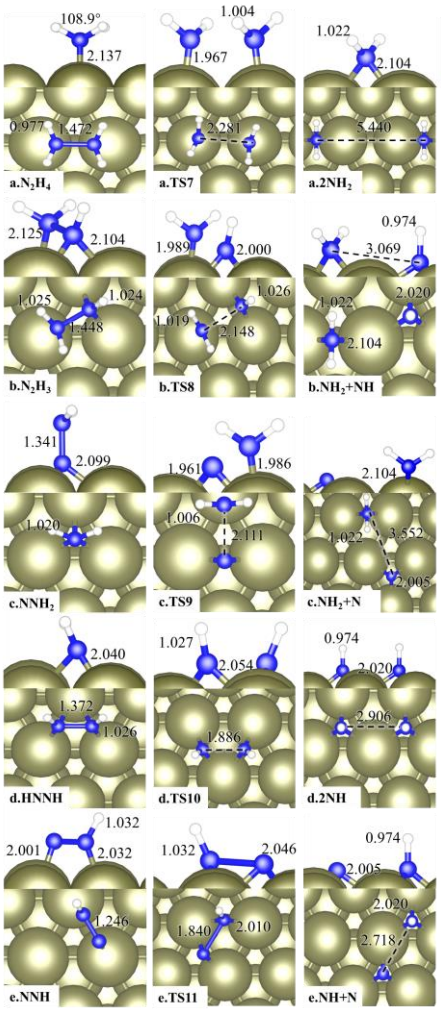

Figure 9. Top and side views of the initial, transition and final states for the dissociation pathway of (a) N_2H_4, (b) N_2H_3, (c) NNH_2, (d) HNNH and (e) NNH. All inset distances are in Å. Blue spheres represent N atoms, white is hydrogen, and Ir is the large green sphere.

Intermolecular dehydrogenation. Upon dissociation of N–N intermediates, the NH_x (x= 1-3) species may assist the dehydrogenation process of co-adsorbed species, i.e. having higher nucleophilicity to drive the proton transfer. Indeed, previously we showed the N-dissociation to be energetically favorable over dehydrogenation, and consequently, the produced NH_2 can withdraw H from co-adsorbed N_2H_x (x= 1-4) intermediates forming NH_3, see ***Figure 10***.

The co-adsorption of NH_2 at a distance of 3.674 Å from N_2H_4 destabilizes the system by 0.13 eV compared with isolated species. The intermolecular dehydrogenation proceeds through a barrier of only 0.20 eV with an energy gain of E_r= -0.47 eV. Similarly, the co-adsorption of other species is destabilized by around 0.2 eV. Assisted dehydrogenation processes have energy barriers smaller than 0.55 eV, except for asymmetric N_2H_2 (E_a= 1.02 eV). This mechanism is driven by the formation of NH_3 and the most likely to take place once NH_2 is present on the surface (see ***Table 3*** and ***Figure 15***).

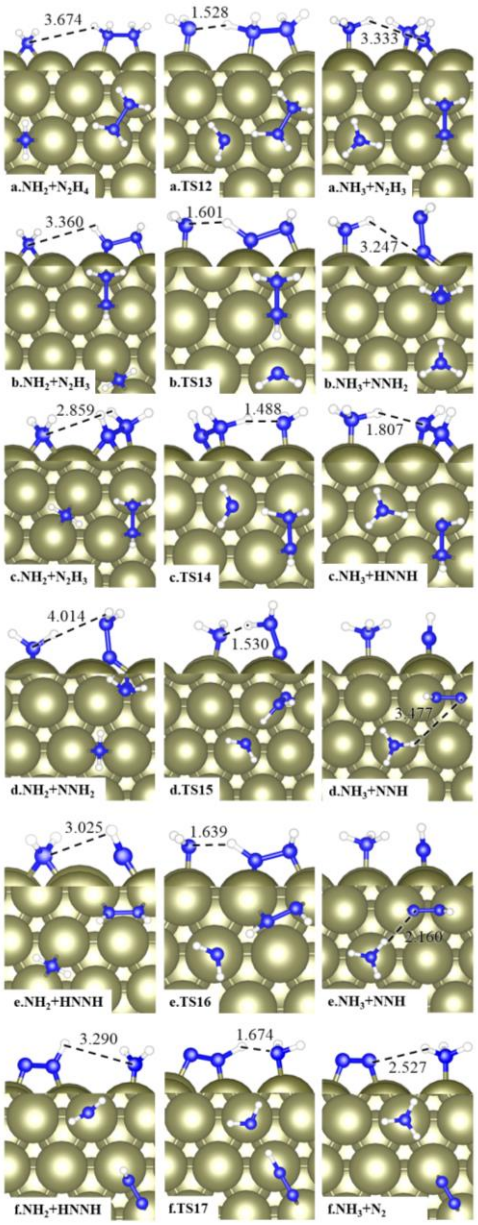

Figure 10. Top and side views of the initial, transition and final states for N2Hx (x= 1-4) attacked by NH_2. (a) N_2H_4 to N_2H_3, (b) N_2H_3 to NNH_2, (c) N_2H_3 to HNNH, (d) NNH_2 to NNH, (e) HNNH to NNH and (e) NNH to N_2. All inset distances are in Å. Blue spheres represent N atoms, white is hydrogen, and Ir is the large green sphere.

We have also studied the NH_2 assisted dehydrogenation of NH_2 and NH_x (x= 1-2) species leading to NH_3, see ***Figure 11***. The process between two NH_2 has a driving energy of -0.59 eV upon overtaking a small energy barrier of 0.34 eV. The barrier of the interaction between NH_2 and NH is kinetically limiting (E_a= 0.98 eV) with the reaction energy of -0.91 eV. As the barrier energy of reaction between NH_2 is relatively higher than with N_2H_4, by 0.14 eV, NH_2 prefers reacting with N_2H_4 instead of NH_2.

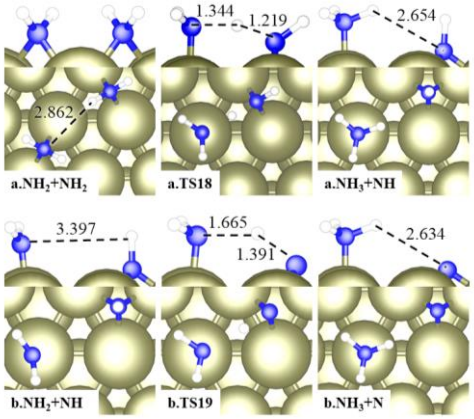

Figure 11. The top and side view of the initial, transition and final states for the interaction of NH_2 molecules. (a) NH_2 and (b) NH. All inset distances are in Å. Blue spheres represent N atoms, white is hydrogen, and Ir is the large green sphere.

NH_x dehydrogenation. Several steps lead to the formation of NH_x (x = 1-3) species. These species may undertake further dehydrogenations leading to a complete decomposition into N_2 and H_2, see ***Figure 12***. Starting with NH_3, its first N–H bond scission needs to overcome a barrier energy of 1.79 eV to produce co-adsorbed NH_2 and H at 0.76 eV above the initial state. In the cases of NH_2 and NH, the dehydrogenation steps are also unlikely due to their high barrier energies 1.96 eV and 1.18 eV, respectively. While these barriers are relatively small compared to the ones found on Cu(111),[24] Rh(111),[15] Pt(111),[36] Ir(100).[37] In line with previous benchmarks, hydrogen ad-atoms easily combine with NH_2 that eventually yield NH_3 molecules.

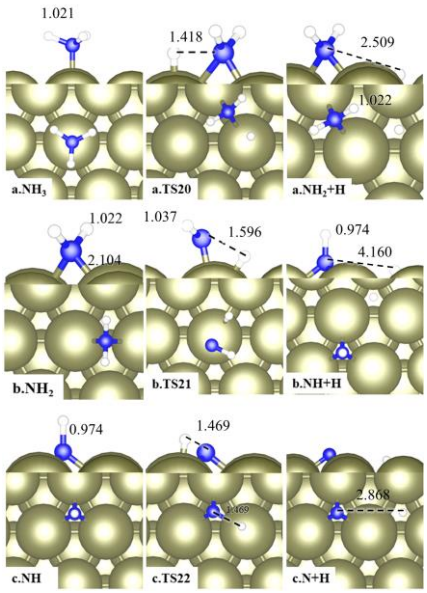

Figure 12. Top and side views of the initial, transition and final states for NH_3 dehydrogenation, (a) NH_3 decomposition, (b) NH_2 decomposition (c) NH decomposition. All inset distances are in Å. Blue spheres represent N atoms, white is hydrogen, and Ir is the large green sphere.

Table 3. Reaction (E_r) and barrier (E_a) energies for the forward and reverse reaction steps. * denotes the adsorbed state, E_r values of the adsorption and desorption processes are equal to the E_{ads} values (i.e. relative to the gas-phase), and υ is the imaginary frequencies of the transition states.

Reactions		Ir (111)			
		E_r (eV)	E_a forward (eV)	E_a reverse (eV)	υ (cm^{-1})
Adsorption-desorption					
R1	$N_2H_4 \leftrightarrow N_2H_4$*	-2.7			
R2	NH_3* $\leftrightarrow NH_3$	1.90			
R3	N_2* $\leftrightarrow N_2$	1.14			
R4	H_2* $\leftrightarrow H_2$	1.37			
Dehydrogenation					
R5	N_2H_4* $\leftrightarrow N_2H_3$*+H*	0.18	1.08	0.91	956.9
R6	N_2H_3* $\leftrightarrow NNH_2$*+H*	0.57	1.02	0.45	482.8
R7	N_2H_3* $\leftrightarrow$ HNNH*+H*	0.54	2.05	1.51	1126.8
R8	HNNH* $\leftrightarrow$ NNH* + H*	-0.19	0.70	0.89	1115.8
R9	NNH_2* $\leftrightarrow$ NNH* + H*	0.11	0.83	0.72	386.1
R10	NNH* $\leftrightarrow$ N_2* + H*	-0.02	1.31	1.33	910.2
N-N dissociation					
R11	N_2H_4* $\leftrightarrow 2NH_2$*	-0.52	0.71	1.23	154.3
R12	N_2H_3* $\leftrightarrow NH_2$*+NH*	-0.71	0.78	1.48	356.9
R13	NNH_2* $\leftrightarrow NH_2$* + N*	-0.53	0.73	1.26	398.7
R14	NHNH* $\leftrightarrow$ 2NH*	-1.49	0.73	2.22	549.7
R15	NNH* $\leftrightarrow$ NH* + N*	-1.21	1.43	2.64	571.9
Intermolecular dehydrogenation					
R16	N_2H_4* + NH_2* $\leftrightarrow$ N_2H_3* + NH_3*	-0.47	0.20	0.67	335.8
R17	N_2H_3* + NH_2* $\leftrightarrow$ HNNH* + NH_3*	-0.13	0.23	0.36	268.3
R18	HNNH* + NH_2* $\leftrightarrow$ NNH* + NH_3*	-1.03	0.19	1.22	322.9
R19	N_2H_3* + NH_2* $\leftrightarrow$ NNH_2* +NH_3*	-0.28	0.37	0.64	252.5
R20	NNH_2* + NH_2* $\leftrightarrow$ NNH* +NH_3*	-0.49	1.02	1.5	654.9
R21	NNH* + NH_2* $\leftrightarrow$ N_2* + NH_3*	-1.35	0.55	1.89	1291.0
NH_x (x = 1,2,3) dehydrogenation					
R22	NH_3* $\leftrightarrow$ NH_2* + H*	0.76	1.79	1.03	1229.5
R23	NH_2* $\leftrightarrow$ NH* + H*	1.66	1.96	0.30	1274.3
R24	NH* $\leftrightarrow$ N* + H*	0.07	1.18	1.12	1154.5
Interaction of NH_2 intermediates					

R25	$2NH_2^* \leftrightarrow NH^* + NH_3^*$	-0.59	0.34	0.93	124.1
R26	$NH^* + NH_2^* \leftrightarrow N^* + NH_3^*$	-0.91	0.98	1.89	213.9
N_2 generation					
R27	$2N^* \leftrightarrow N_2^*$	-0.59	2.02	2.61	568.3
H_2 generation					
R28	$2H^* \leftrightarrow H_2^*$	0.31	0.51	0.20	271.1

From the analysis of the previous reaction pathways, we conclude that the primary mechanism for the N_2H_4 decomposition on Ir(111) is the intermolecular dehydrogenation once NH_2 is on the surface. It implies that the N–N scission also takes place. These two mechanisms yield N_2 and NH_3 from a single N_2H_4 molecule under mild condition, in line with the experiments.[38]

4.4 Desorption of products

Previously, we described the favorable formation of NH_3 *via* N–N scission and dehydrogenation pathways. These mechanisms may also generate N and H ad-atoms on the surface, which recombination yield N_2 and H_2 molecules. The formation of an N_2 molecule is exothermic by 0.59 eV but has an energy barrier of 2.02 eV. On the other hand, the formation of H_2 is endothermic by 0.31 eV with an accessible barrier of 0.51 eV. These simple thermodynamic analyses agree with previous results in which NH_3 was observed at temperatures as low as 150 °C, temperatures above 200 °C were necessary to observe H_2.[5,8]

4.5 Energy profiles

We summarized the energy profiles of the three reaction mechanisms in ***Figure 13***, ***Figure 14*** and ***Figure 15***. The first figure contains the two different pathways for intramolecular dehydrogenation; the second is analysis of the intermolecular dehydrogenation pathway between NH_2 and N_2H_4, and the last one depicts the dehydrogenation reactions between NH_2 from N–N scission.

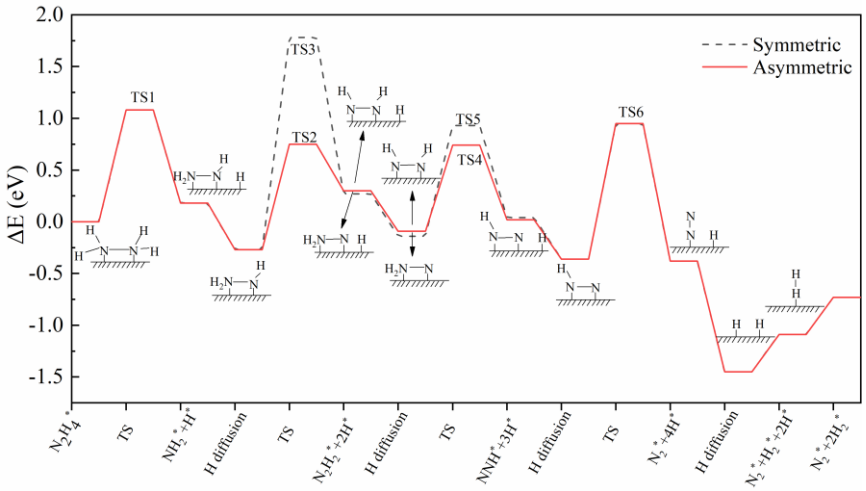

Figure 13. Intramolecular dehydrogenation pathways of N_2H_4 dissociation over the Ir(111) surface. TS indicates the energy of the transition energies.

According to ***Table 3*** and ***Figure 13***, the reaction R7 (N_2H_3*↔HNNH*+H is the dominant reaction barrier (TS3) for the intramolecular symmetry dehydrogenation pathway with an energy of 2.05 eV. The only step to generate N_2, R10, has a limiting barrier (TS6) of 1.31 eV, whereas hydrogen desorption energy is 1.37 eV. These energy requirements are higher than those found in the NH_2 assisted dehydrogenation pathway.

According to the DOS and thermodynamics analyses (***Table 3***, ***Figure 6*** and ***Figure 15***), N-N bond breakage is the prevailing pathway through the whole decomposition process and produces NH_2, NH and N fragments (R11, R12, R13 and R14) with relatively low reaction energies and barriers, which may assist the dehydrogenation process on co-adsorbed N_2H_4. The large energy barrier of 1.96 eV, TS21 in ***Figure 15***, favors the existence of NH_2 on the surface.

The intermolecular NH_2 assisted dehydrogenation (R16-21) of N_2H_4 (***Figure 14***) may produce large amounts of NH_3 as its dehydrogenation (R22) is largely endothermic (E_r= 0.76 eV). Indeed, an assisted symmetric dehydrogenation step is thermodynamically favorable with energy barriers (TS12-15) no more than 0.55 eV. The assisted dehydrogenation will yield N_2 from undissociated N_2H_4 molecules in agreement with isotopic data.[38]

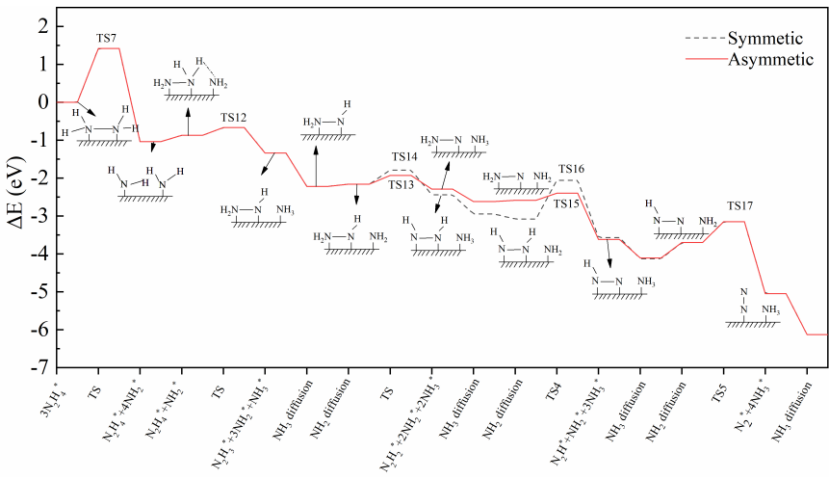

Figure 14 . Intermolecular dehydrogenation of hydrazine via NH_2 attack pathways over the Ir(111) surface. TS indicates the energy of the transition energies.

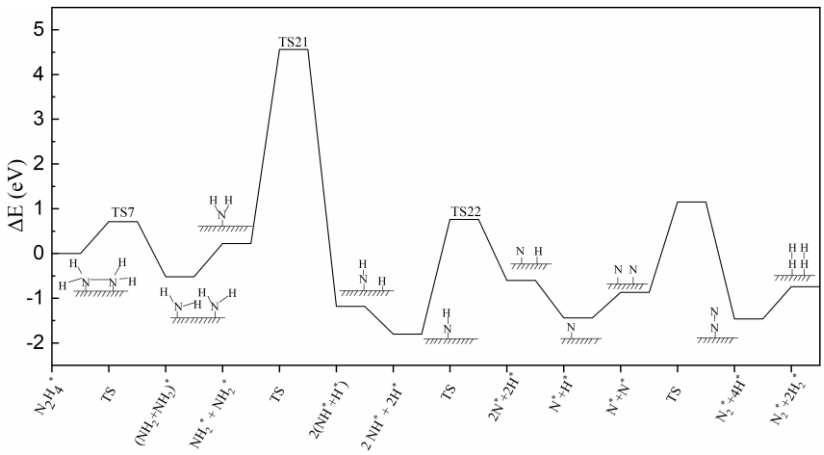

Figure 15. N-N bond breaking and subsequent dehydrogenation pathways of N_2H_4 dissociation over the Ir(111) surface. TS indicates the energy of the transition energies.

In summary, N_2H_4 tends to split into NH_2 early in the decomposition process. These intermediates assist the dehydrogenation of co-adsorbed N_2H_x (x = 1-4) species yielding NH_3 and N_2 molecules. The crucial role of NH_2 in the selectivity control agrees with the mechanism on Ir(100),[37] Cu(111),[14] Rh(111),[15] Pt(111).[36] At higher temperatures, the competitive intramolecular dehydrogenation pathway generate molecular hydrogen, consistent with experimental studies.[39] While at low temperature, reduced Ir/CeO_2 exhibits a yield toward hydrogen formation of 0.73% ± 0.12% in our experiment.

4.6 Infrared spectra

Infrared spectroscopy (IR) plays an important role in the characterization of the catalytic process, due to its ability to identify intermediate species along with the reaction mechanisms. We derived the spectra of the different adsorbed species present during the dehydrogenation of hydrazine. ***Figure 16a*** shows that the strength of the hydrogen vibrations decreases with the dehydrogenation, and the peak associated with the N-N vibration has an obvious red-shift in the spectrum.[40-41] This shift indicates that the dehydrogenation process will make the N-N bond stronger, increasing the bond order, in agreement with the dissociation energies R11 – R15. ***Figure 16b*** shows the spectra derived from the species with a single nitrogen atom, i.e. NH_3, NH_2, NH and N. The distinctive stretching of ammonia is at 1010.8 cm^{-1},[42] which shift to lower wavenumbers with the dehydrogenation species becoming IR-active at 750 cm^{-1} for NH intermediate.

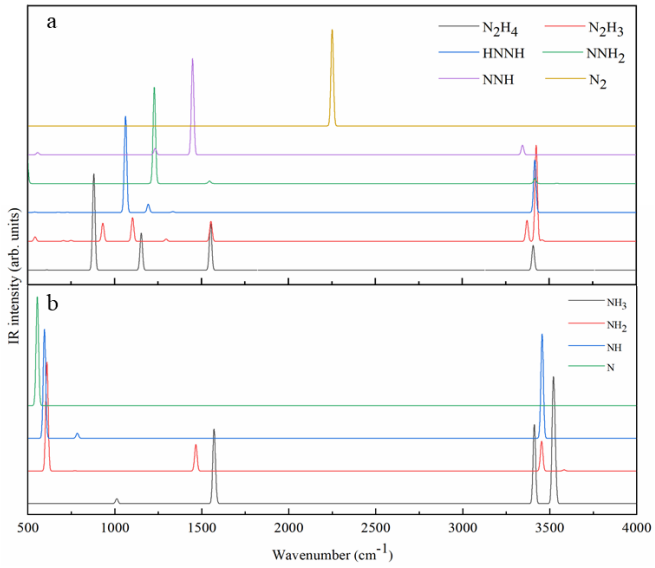

Figure 16. a) Infrared spectra for adsorbate N_2H_4, N_2H_3, HNNH, NNH_2, NNH and N_2); b) Infrared spectra for adsorbate NH_3, NH_2, NH and N

5 Conclusions

We have combined computational and experimental techniques to compare the adsorption process of hydrazine and products of its decomposition on Ir(111) and IrO_2 surfaces. We found that the strong molecular adsorptions on IrO_2 block the catalytic site. We followed the catalytic pathways and decomposition mechanisms of N_2H_4 decomposition on Ir(111) using density functional theory (DFT) calculations. We have studied the electron density and density of states (DOS) of the hydrazine adsorbate system and explained the N-N bond scission by the molecular orbital theory. Furthermore, we analysis the vibrations of hydrazine, NH_3 and their intermediates to support the experimental findings from infrared spectra. Intermediate adsorptions were followed by the analysis of three catalytic mechanisms (intramolecular reaction between hydrazine, the intramolecular reaction between NH_2, and NH_2 assisted dehydrogenation). The results show that hydrazine decomposition prefers to start with an initial N-N bond scission toward an NH_2 intermediate, which facilitates the subsequent dehydrogenation from N_2H_x (x = 1-4) to produce N_2 and NH_3. It is challenging to produce hydrogen ad-atoms by N-H bond breaking and perform recombination of hydrogen molecules at moderate temperatures because of the high activation barriers and reaction energies. Therefore, it can be understood from our calculations that at ambient conditions, the main products are NH_3 and N_2, as supported by experimental work, and that controlling the antibonding molecular orbital (π^*) occupation may lead to a more selective decomposition towards molecular hydrogen.

6. Acknowledgements

X. Lu acknowledges the China Scholarship Council and Cardiff University for the overseas student scholarship. We are grateful for funding by the Engineering & Physical Sciences Research Council (EP/P005845/1). Via our membership of the UK's HPC Materials Chemistry Consortium, which is funded by EPSRC (EP/L000202), this work used the UK Materials and Molecular Modelling Hub for computational resources, MMM Hub, which is partially funded by EPSRC (EP/P020194). We also acknowledge computing time on the facilities of HPC Wales and the Advanced Research Computing @ Cardiff (ARCCA) at Cardiff University. All data created during this research are openly available from the University of Cardiff Research Portal http://doi.org/10.17035/d.2019.0087115515.

7. References

(1) Smith, M. J.; Alabi, O.; Hughes, N.; Dodds, P. E.; Turner, K.; Irvine, J. T. The Economic Impact of Hydrogen and Fuel Cells in the UK. *H2FC Supergen, London, UK* **2017**.

(2) Hayashi, H. Hydrazine Synthesis: Commercial Routes, Catalysis and Intermediates. *Research on chemical intermediates* **1998**, *24* (2), 183–196.

(3) Schirmann, J.-P. Method for Preparing Hydrazine Hydrate, February 2003.

(4) Qiao, S.; Yin, X.; Tian, T.; Jin, R.; Zhou, J. Hydrazine Production by Anammox Biomass with NO Reversible Inhibition Effects. *Green Chemistry* **2016**, *18* (18), 4908–4915.

(5) Aika, K.; Ohhata, T.; Ozaki, A. Hydrogenolysis of Hydrazine over Metals. *Journal of Catalysis* **1970**, *19* (2), 140–143.

(6) Rehse, K.; Shahrouri, T. Hydrazine Derivatives. *Archiv der Pharmazie: An International Journal Pharmaceutical and Medicinal Chemistry* **1998**, *331* (10), 308–312.

(7) Schulz-Ekloff, G.; Hoppe, R. Electron Diffraction Determination of an Orientation-Relationship for Iridium-on-η-Alumina. *Catal Lett* **1990**, *6* (3), 383–387. https://doi.org/10.1007/BF00764005.

(8) Cho, S. J.; Lee, J.; Lee, Y. S.; Kim, D. P. Characterization of Iridium Catalyst for Decomposition of Hydrazine Hydrate for Hydrogen Generation. *Catalysis letters* **2006**, *109* (3–4), 181–186.

(9) Singh, S. K.; Xu, Q. Complete Conversion of Hydrous Hydrazine to Hydrogen at Room Temperature for Chemical Hydrogen Storage. *Journal of the American Chemical Society* **2009**, *131* (50), 18032–18033.

(10) Singh, S. K.; Zhang, X.-B.; Xu, Q. Room-Temperature Hydrogen Generation from Hydrous Hydrazine for Chemical Hydrogen Storage. *Journal of the American Chemical Society* **2009**, *131* (29), 9894–9895.

(11) Singh, S. K.; Iizuka, Y.; Xu, Q. Nickel–Palladium Nanoparticle Catalyzed Hydrogen Generation from Hydrous Hydrazine for Chemical Hydrogen Storage. *International Journal of Hydrogen Energy* **2011**, *36* (18), 11794–11801.

(12) Manukyan, K. V.; Cross, A.; Rouvimov, S.; Miller, J.; Mukasyan, A. S.; Wolf, E. E. Low Temperature Decomposition of Hydrous Hydrazine over FeNi/Cu Nanoparticles. *Applied Catalysis A: General* **2014**, *476*, 47–53.

(13) Block, J.; Schulz-Ekloff, G. The Catalytic Decomposition of Nitrogen-15-Labeled Hydrazine on MgO-Supported Iron. *Journal of Catalysis* **1973**, *30* (2), 327–329.

(14) Tafreshi, S. S.; Roldan, A.; de Leeuw, N. H. Density Functional Theory Calculations of the Hydrazine Decomposition Mechanism on the Planar and Stepped Cu(111) Surfaces. *Phys. Chem. Chem. Phys.* **2015**, *17* (33), 21533–21546. https://doi.org/10.1039/C5CP03204K.

(15) Deng, Z.; Lu, X.; Wen, Z.; Wei, S.; Liu, Y.; Fu, D.; Zhao, L.; Guo, W. Mechanistic Insight into the Hydrazine Decomposition on Rh (111): Effect of Reaction Intermediate on Catalytic Activity. *Physical Chemistry Chemical Physics* **2013**, *15* (38), 16172–16182.

(16) Zhang, P.-X.; Wang, Y.-G.; Huang, Y.-Q.; Zhang, T.; Wu, G.-S.; Li, J. Density Functional Theory Investigations on the Catalytic Mechanisms of Hydrazine Decompositions on Ir(111). *Catalysis Today* **2011**, *165* (1), 80–88. https://doi.org/10.1016/j.cattod.2011.01.012.

(17) Grimme, S.; Antony, J.; Ehrlich, S.; Krieg, H. A Consistent and Accurate Ab Initio Parametrization of Density Functional Dispersion Correction (DFT-D) for the 94 Elements H-Pu. *The Journal of chemical physics* **2010**, *132* (15), 154104.

(18) Kresse, G.; Furthmüller, J. Efficiency of Ab-Initio Total Energy Calculations for Metals and Semiconductors Using a Plane-Wave Basis Set. *Computational materials science* **1996**, *6* (1), 15–50.

(19) Bucko, T.; Hafner, J.; Lebegue, S.; Angyán, J. G. Improved Description of the Structure of Molecular and Layered Crystals: Ab Initio DFT Calculations with van Der Waals Corrections. *The Journal of Physical Chemistry A* **2010**, *114* (43), 11814–11824.

(20) Perdew, J. P.; Burke, K.; Ernzerhof, M. Generalized Gradient Approximation Made Simple. *Physical review letters* **1996**, *77* (18), 3865.

(21) Perdew, J. P.; Ruzsinszky, A.; Csonka, G. I.; Vydrov, O. A.; Scuseria, G. E.; Constantin, L. A.; Zhou, X.; Burke, K. Restoring the Density-Gradient Expansion for Exchange in Solids and Surfaces. *Physical review letters* **2008**, *100* (13), 136406.

(22) Kresse, G.; Joubert, D. From Ultrasoft Pseudopotentials to the Projector Augmented-Wave Method. *Physical review b* **1999**, *59* (3), 1758.

(23) Grimme, S.; Ehrlich, S.; Goerigk, L. Effect of the Damping Function in Dispersion Corrected Density Functional Theory. *Journal of computational chemistry* **2011**, *32* (7), 1456–1465.

(24) Tafreshi, S. S.; Roldan, A.; Dzade, N. Y.; de Leeuw, N. H. Adsorption of Hydrazine on the Perfect and Defective Copper (111) Surface: A Dispersion-Corrected DFT Study. *Surface Science* **2014**, *622*, 1–8.

(25) Dzade, N.; Roldan, A.; de Leeuw, N. A Density Functional Theory Study of

the Adsorption of Benzene on Hematite (α-Fe2O3) Surfaces. *Minerals* **2014**, *4* (1), 89–115.

(26) Roldan, A.; de Leeuw, N. H. A Kinetic Model of Water Adsorption, Clustering and Dissociation on the Fe3S4{001} Surface. *Physical Chemistry Chemical Physics* **2017**, *19* (19), 12045–12055.

(27) Singh, H. P. Determination of Thermal Expansion of Germanium, Rhodium and Iridium by X-Rays. *Acta Crystallographica Section A: Crystal Physics, Diffraction, Theoretical and General Crystallography* **1968**, *24* (4), 469–471.

(28) Mills, G.; Jónsson, H. Quantum and Thermal Effects in H 2 Dissociative Adsorption: Evaluation of Free Energy Barriers in Multidimensional Quantum Systems. *Physical review letters* **1994**, *72* (7), 1124.

(29) Mills, G.; Jónsson, H.; Schenter, G. K. Reversible Work Transition State Theory: Application to Dissociative Adsorption of Hydrogen. *Surface Science* **1995**, *324* (2–3), 305–337.

(30) Heyden, A.; Bell, A. T.; Keil, F. J. Efficient Methods for Finding Transition States in Chemical Reactions: Comparison of Improved Dimer Method and Partitioned Rational Function Optimization Method. *The Journal of chemical physics* **2005**, *123* (22), 224101.

(31) Freakley, S. J.; Ruiz-Esquius, J.; Morgan, D. J. The X-Ray Photoelectron Spectra of Ir, IrO2 and IrCl3 Revisited. *Surface and Interface Analysis* **2017**, *49* (8), 794–799. https://doi.org/10.1002/sia.6225.

(32) Matz, O.; Calatayud, M. Periodic DFT Study of Rutile IrO2: Surface Reactivity and Catechol Adsorption. *The Journal of Physical Chemistry C* **2017**, *121* (24), 13135–13143.

(33) Schmidt, E.; W, E. Oxidation Resistance of Hydrazine Decomposition Catalysts, Part I: Alumina-Supported Iridium Catalyst. *Oxidation of Metals* **1975**.

(34) Agusta, M. K.; Kasai, H. First Principles Investigations of Hydrazine Adsorption Conformations on Ni(111) Surface. *Surface Science* **2012**, *606* (7), 766–771. https://doi.org/10.1016/j.susc.2012.01.009.

(35) Hoffmann, R. A Chemical and Theoretical Way to Look at Bonding on Surfaces. *Rev. Mod. Phys.* **1988**, *60* (3), 601–628. https://doi.org/10.1103/RevModPhys.60.601.

(36) Rosca, V.; Koper, M. T. M. Electrocatalytic Oxidation of Ammonia on Pt(111) and Pt(100) Surfaces. *Phys. Chem. Chem. Phys.* **2006**, *8* (21), 2513–2524. https://doi.org/10.1039/B601306F.

(37) Huang, W.; Lai, W.; Xie, D. First-Principles Study of Decomposition of NH3 on Ir(100). *Surface Science* **2008**, *602* (6), 1288–1294. https://doi.org/10.1016/j.susc.2008.01.029.

(38) Maurel, R.; Menezo, J. C. Catalytic Decomposition of 15N-Labeled Hydrazine on Alumina-Supported Metals. *Journal of Catalysis* **1978**, *51* (2), 293–295. https://doi.org/10.1016/0021-9517(78)90304-4.

(39) Al-Haydari, Y. K.; Saleh, J. M.; Matloob, M. H. Adsorption and

Decomposition of Hydrazine on Metal Films of Iron, Nickel, and Copper. *The Journal of Physical Chemistry* **1985**, *89* (15), 3286–3290.

(40) Durig, J. R.; Griffin, M. G.; Macnamee, R. W. Raman Spectra of Gases. XV: Hydrazine and Hydrazine-D4. *Journal of Raman Spectroscopy* **1975**, *3* (2–3), 133–141. https://doi.org/10.1002/jrs.1250030204.

(41) Yamaguchi, A.; Ichishima, I.; Shimanouchi, T.; Mizushima, S.-I. Far Infra-Red Spectrum of Hydrazine. *Spectrochimica Acta* **1960**, *16* (11–12), 1471–1485.

(42) Koops, Th.; Visser, T.; Smit, W. M. A. Measurement and Interpretation of the Absolute Infrared Intensities of NH3 and ND3. *Journal of Molecular Structure* **1983**, *96* (3), 203–218. https://doi.org/10.1016/0022-2860(83)90049-2.